applied sciences

MDPI

Article

Experimental Investigation of Sandstone Damage Evolution and Failure Mechanisms Under Freeze–Thaw Cycles

Jianxi Ren, Kechen Zhang, Mengchen Yun *, Zhengtao Jiang and Haojun Wang

School of Architecture and Civil Engineering, Xi'an University of Science and Technology, Xi'an 710054, China; renjianxi1968@163.com (J.R.); yntuzh@outlook.com (K.Z.); 19880212434@163.com (Z.J.); 19838206206@163.com (H.W.)

* Correspondence: yunmc1019@163.com

Abstract

Elucidating the evolution of sandstone pore structure and the mechanisms of macroscopic damage and failure under freeze–thaw cycling is an important scientific issue for the safe construction and operation of rock engineering projects in cold regions. In this study, sandstone collected from a slope along the Qinghai–Tibet Railway in a seasonally frozen region of western China was investigated. Micro-, meso-, and macroscale experiments were conducted on sandstone specimens subjected to different numbers of freeze–thaw cycles. Scanning electron microscopy (SEM), nuclear magnetic resonance (NMR), computed tomography (CT), and digital image correlation (DIC) were employed to investigate changes in the physical and mechanical properties, pore structure evolution, and macroscopic fracture characteristics of sandstone. Freeze–thaw cycling continuously weakened intergranular cementation and promoted the propagation and interconnection of microcracks. Meanwhile, the pore structure gradually shifted from micropores ($r < 0.1$ μm) toward mesopores (0.1 μm $\leq r < 10$ μm) and macropores ($r \geq 10$ μm). With increasing numbers of freeze–thaw cycles, the total number of pores identified by CT decreased from 256,237 to 194,910, whereas the number of connected pores increased from 222 to 1308. The connected porosity increased from 2.25% to 10.40%, the gas-measured porosity increased from 10.63% to 12.45%, and the permeability increased from 0.28 mD to 0.96 mD. In addition, the dry mass of the monitored specimen decreased from 464.53 g to 461.52 g, representing a reduction of 0.65%. The P-wave velocity decreased from 2.632 km/s to 2.309 km/s, corresponding to a reduction of 12.30%. During uniaxial compression, strain localization became more pronounced with increasing freeze–thaw damage. The high-strain zones observed by DIC, defined as regions of localized strain concentration, gradually expanded from localized concentrations to multiple regions, ultimately leading to specimen failure. The results indicate that freeze–thaw damage is essentially a progressive process involving the activation of microdefects, pore expansion and coalescence, crack interconnection, and reconstruction of the interconnected pore network, ultimately resulting in the continuous deterioration of the structural integrity of sandstone.

Keywords: freeze–thaw cycles; sandstone; CT scanning; pore structure; damage deterioration

Academic Editor: Claudio Mazzotti

Received: 28 September 2026
Revised: 26 October 2026
Accepted: 28 October 2026
Published: 30 October 2026

Copyright: © 2026 by the authors. Licensee MDPI, Basel, Switzerland. This article is an open access article distributed under the terms and conditions of the Creative Commons Attribution (CC BY) license.

1. Introduction

Climate change is altering temperature conditions and freeze–thaw regimes in cold regions. These changes significantly affect the long-term stability of rock engineering structures and infrastructure. For rock slopes in cold regions, repeated freeze–thaw cycles cause water in pores and fractures to undergo cyclic water–ice phase transitions. Frost-heaving pressure generated during freezing and moisture migration during thawing promote the expansion and interconnection of pores and microcracks within the rock. As damage accumulates, the structural integrity and mechanical properties of the rock progressively deteriorate. Consequently, the risks of rock deformation, localized failure, and slope instability increase, seriously threatening the long-term stability of engineering structures in cold regions [1–6]. Environmental changes associated with climate change may also affect material degradation and, consequently, the long-term service performance of engineering structures.

Numerous studies have shown that freeze–thaw damage in rocks is essentially a process of continuous development and deterioration of the internal pore and fracture structure. During the freezing stage, the phase transition and expansion of pore water exert frost-heaving effects on the pore walls and grain-cementation interfaces, whereas during the thawing stage, water migrates and replenishes the expanded pore spaces. Consequently, under repeated freeze–thaw action, pre-existing pore defects within the rock continuously expand, coalesce, and interconnect, causing the pore structure to gradually transform from a state of discrete pores to one characterized by interconnected fractures. This process ultimately manifests as mass loss, decreased P-wave velocity, increased porosity, and deterioration of mechanical properties [7,8].

With the development of microscale characterization techniques, scanning electron microscopy (SEM), nuclear magnetic resonance (NMR), and computed tomography (CT) have been increasingly applied to studies of freeze–thaw-induced damage in rocks. SEM enables direct observation of changes in mineral grains, cementation structures, and microcracks, revealing that freeze–thaw action can weaken intergranular cementation and promote crack propagation [9,10]. NMR enables non-destructive characterization of the pore structure of rocks. Previous studies have shown that freeze–thaw cycles can alter the T_2 spectrum distribution, promote the transition of small pores toward medium- and large-sized pores, and enhance pore connectivity [11,12]. Combined with fractal theory, NMR can further be used to evaluate the complexity of the pore structure. CT scanning enables three-dimensional reconstruction of the internal pore structure and quantitative characterization of porosity, pore size, and connectivity characteristics, providing an effective means of analyzing the evolution of the pore network during freeze–thaw cycling [13–15].

In addition to the evolution of the internal pore structure, freeze–thaw damage also significantly affects the deformation and failure behavior of rocks under loading. Digital image correlation (DIC) enables continuous acquisition of full-field strain information during uniaxial loading of rocks and can effectively identify crack initiation, propagation, and strain localization characteristics [16–18]. In recent years, DIC has been increasingly applied to studies of freeze–thaw-damaged rocks. Previous studies have shown that, with increasing freeze–thaw damage, localized strain concentration in rocks becomes more pronounced, while high-strain zones expand and gradually develop into continuous failure zones [19–21], providing a new approach for revealing the transition from mesoscale freeze–thaw damage to macroscopic failure.

Considerable progress has been made in research on freeze–thaw-induced rock damage. However, existing studies have mainly focused on specific characteristics at different scales. Scanning electron microscopy (SEM; 20–200 μm) has primarily been used to investigate intergranular cementation and microcracks. Nuclear magnetic resonance (NMR;

0.001–10,000 μm) has been employed to characterize pore-size distributions, while computed tomography (CT; ≥35 μm) has been used to investigate three-dimensional pore networks. At the macroscale, research has focused on the deformation and failure behavior of sandstone under loading. Nevertheless, the mechanisms of pore expansion, coalescence, and coarsening, as reflected by the decrease in pore number and the increases in porosity and pore connectivity during freeze–thaw cycling, require further investigation. Therefore, it is necessary to integrate multiscale characterization techniques to further investigate the evolution of rock pore structure under freeze–thaw action and the relationship between macroscopic and microscopic damage.

Based on the above, sandstone was selected as the research material in this study, and freeze–thaw cycling tests were conducted. Changes in the macroscopic physical properties of the sandstone were analyzed through measurements of mass, P-wave velocity, porosity, and permeability. SEM and NMR were employed to investigate grain cementation and the evolution of pores at different scales. Three-dimensional reconstruction of the sandstone specimens was performed using CT scanning, and a pore network model (PNM) was established to analyze the evolution of pore connectivity, pore size, and permeability characteristics. Finally, uniaxial compression tests combined with DIC were used to characterize strain localization and failure characteristics at different degrees of freeze–thaw damage. Through these multiscale analyses, the damage deterioration of the microscopic pore structure and the macroscopic deformation and failure mechanisms of sandstone specimens under freeze–thaw action were comprehensively investigated, providing a theoretical basis for the freeze–thaw damage assessment and stability analysis of rock engineering structures in cold regions.

The main contribution of this study lies in the integration of multiscale characterization techniques, including SEM, NMR, CT, and DIC, to comprehensively investigate the microstructural characteristics, pore network evolution, and macroscopic deformation and failure behavior of sandstone subjected to different numbers of freeze–thaw cycles. Particular attention is paid to the evolution of the pore structure, characterized by a decrease in the total number of pores accompanied by increases in the number and porosity of interconnected pores. The relationships among pore expansion, coalescence, and the reconstruction of interconnected pore networks are further analyzed. In addition, by combining the evolution of DIC strain fields, this study examines the relationship between internal pore structure deterioration and the development of strain localization and macroscopic failure patterns during loading. These findings provide multiscale experimental evidence for understanding the progressive transition from microstructural deterioration to macroscopic failure in sandstone subjected to freeze–thaw cycles.

2. Materials and Methods

2.1. Specimen Preparation

The sandstone used in this study was collected from a slope along the Qinghai–Tibet Railway in Qinghai Province, China. To minimize the initial differences among rock cores used in different experiments, sandstone blocks were collected from adjacent locations within the same rock stratum. Intact sandstone blocks without visible cracks or weathering defects were selected as the parent rock. The sandstone blocks were subsequently subjected to core drilling, core cutting, surface grinding, and P-wave velocity screening to prepare standard cylindrical specimens of φ50 × 100 mm. Basic parameters, including mass, density, and P-wave velocity, were measured, and specimens with similar initial physical properties were selected for different experiments to minimize the influence of specimen-to-specimen variations on the experimental results. The detailed specimen preparation procedure is shown in Figure 1.



(**a**) Core drilling (**b**) Core cutting (**c**) Surface grinding (**d**) Specimen selection

Figure 1. Preparation procedure for standard cylindrical rock specimens.

2.2. Experimental Scheme

(1) Freeze–thaw cycling test scheme

Freeze–thaw cycling tests were conducted using a JCD-40 intelligent numerical-control freeze–thaw testing machine(Beijing, China). Considering the annual climatic characteristics of the seasonally frozen region in western China (Figure 2) [22], an "air-freezing–water-thawing" method was adopted for the freeze–thaw cycling treatment. The freezing temperature was set at −20 °C with a freezing duration of 4 h, while the thawing temperature was set at 20 °C with a thawing duration of 4 h. The temperature change rate was set at 40 °C/h. The procedure of the freeze–thaw cycling test is shown in Figure 3.

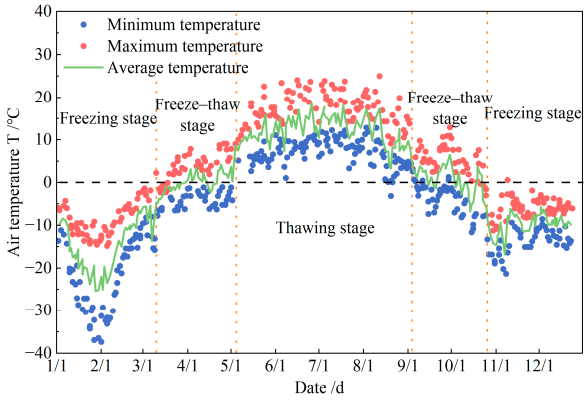


Figure 2. Annual climatic characteristics of seasonal frozen regions in western China.

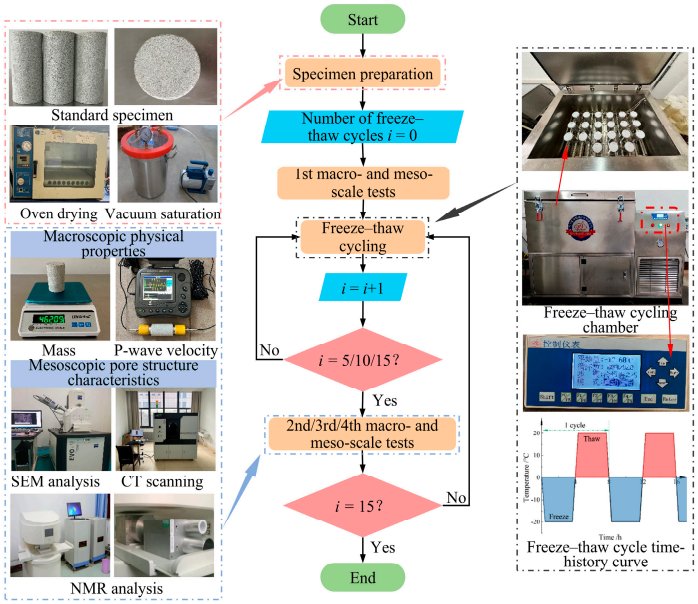
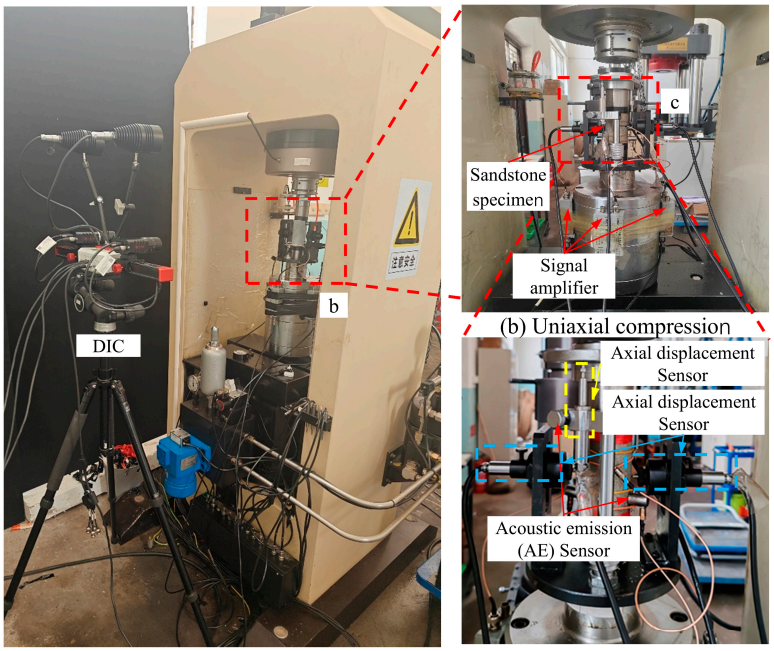


Figure 3. Flowchart of the freeze–thaw cycle test procedure.

(2) Uniaxial compression test scheme

Uniaxial compression tests were conducted using an RMT−201 rock mechanics testing system consisting of a loading system and a data acquisition system, with a maximum axial load capacity of 1500 kN. The tests were performed at room temperature under displacement-controlled loading at a rate of 0.001 mm/s. Loading was continued until visible macroscopic failure of the sandstone specimens occurred, at which point the tests were terminated. Load and deformation data were recorded throughout the loading process. The uniaxial compression test procedure is shown in Figure 4.



(a) RMT-201 rock mechanics testing system (c) Sensor installation for uniaxial compression testing

Figure 4. RMT−201 rock mechanics testing system.

3. Analysis of Experimental Results

3.1. Basic Physical and Mechanical Properties of Sandstone

X-ray diffraction (XRD) results showed that the sandstone used in the experiments was mainly composed of kaolinite (46.3%), quartz (31.5%), K-feldspar (approximately 9%), and chlorite (9.5%). Meanwhile, the basic physical parameters of six sandstone specimens were measured, and specimens with the most similar density, P-wave velocity, and saturated water absorption were selected. The basic physical parameters of the selected specimens are presented in Table 1. The specimens had an average saturated mass of 481.82 g, an average dry mass of 465.04 g, an average saturated density of 2.45 g·cm^{-3}, an average dry density of 2.37 g·cm^{-3}, a P-wave velocity of 2.509 km·s^{-1} in the dry state, and an average saturated water absorption of 3.61%.

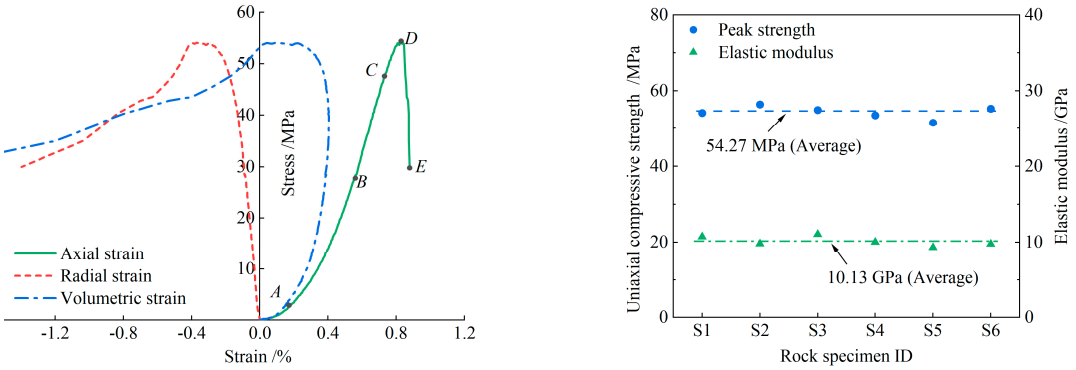
The uniaxial compression test results showed that the peak strength of the sandstone specimens ranged from 51.53 to 56.35 MPa, with an average value of 54.27 MPa. The elastic modulus ranged from 9.33 to 11.07 GPa, with an average value of 10.13 GPa, while the peak strain ranged from 0.79% to 0.85%, with an average value of 0.83% ((Table 2 and Figure 5). These results indicate that the mechanical parameters obtained from the uniaxial compression tests exhibited relatively low variability. Therefore, the corresponding average values can be used to represent the mechanical properties of the sandstone.

Table 1. Physical parameters of intact sandstone specimens.

Specimen No.	Saturated Mass (m)	Dry Mass (m)	Saturated Density (g·cm⁻³)	Dry Density (g·cm⁻³)	Dry P-Wave Velocity (km·s⁻¹)	Saturated Water Absorption (%)
S1	481.96	465.48	2.45	2.37	2.542	3.54
S2	480.99	464.10	2.45	2.36	2.517	3.64
S3	487.01	469.24	2.48	2.39	2.483	3.79
S4	479.95	462.98	2.44	2.36	2.492	3.67
S5	477.81	461.92	2.43	2.35	2.475	3.44
S6	483.22	466.54	2.46	2.38	2.543	3.58
average	481.82	465.04	2.45	2.37	2.509	3.61

Table 2. Uniaxial compression mechanical parameters of intact sandstone specimens.

Specimen No.	Peak Stress σ_f (MPa)	Peak Strain ε_f (%)	Elastic Modulus E (GPa)	Poisson's Ratio μ
S1	54.12	0.83	10.74	0.16
S2	56.35	0.81	9.82	0.17
S3	54.88	0.85	11.07	0.18
S4	53.50	0.84	10.04	0.16
S5	51.53	0.83	9.33	0.16
S6	55.26	0.79	9.80	0.15
average	54.27	0.83	10.13	0.16



(**a**) Uniaxial compression stress–strain curve (**b**) Uniaxial compressive peak strength and elastic modulus

Figure 5. Uniaxial compression test results of intact sandstone specimens. Note: A–E denote characteristic points on the stress–strain curve, and S1–S6 represent the specimen IDs.

3.2. Freeze–Thaw Cycling Tests on Sandstone

3.2.1. Changes in Pore Structure

To reveal the evolution characteristics of the internal pore structure and microcracks of sandstone under freeze–thaw cycles, scanning electron microscopy (SEM) was employed to examine sandstone specimens subjected to different numbers of freeze–thaw cycles. SEM images of the sandstone after different numbers of freeze–thaw cycles were obtained at magnifications of 50×, 100×, and 500×, as shown in Figure 6. It can be observed that the sandstone contains pre-existing pores and microcracks, with cementing materials and fine debris distributed between the grains, providing basic spaces for water to enter and be retained within the rock. Before freeze–thaw cycling, the surfaces of the sandstone grains were relatively smooth, the intergranular cementation was relatively tight, and only a small number of pre-existing pores and microcracks were present, indicating a relatively intact overall structure. After 10 freeze–thaw cycles, cracks between the grains

gradually developed and propagated, transgranular cracks began to appear, and some grains fractured. After 15 freeze–thaw cycles, the intergranular and transgranular cracks developed further. The intergranular cracks within the observed field of view were largely interconnected, the grain surfaces became rough, and grain fracture occurred frequently.

The above results indicate that freeze–thaw cycles continuously promote the propagation of pores and cracks and the deterioration of the cementation structure within the sandstone. The phase-transition expansion and frost-heaving pressure generated by the freezing of pore water promote the propagation of pre-existing defects, while water migration and replenishment during thawing provide conditions for subsequent freezing. After repeated freezing–thawing action, damage in the sandstone gradually shifts from deterioration of the intergranular cementing material to grain failure. Meanwhile, intergranular pores and cracks gradually interconnect and eventually form a complex fracture network, leading to grain fracture and detachment and ultimately resulting in the deterioration of the physical and mechanical properties of the sandstone.

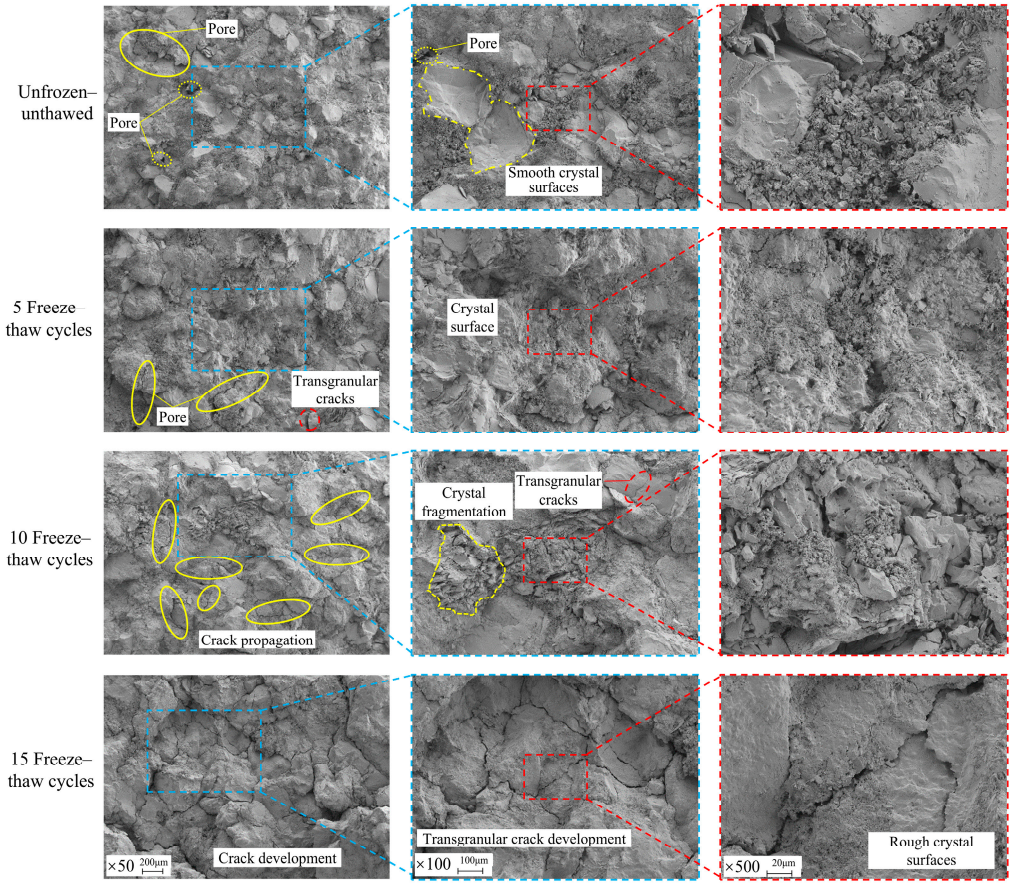


Figure 6. SEM images of the mesostructure of sandstone after different numbers of freeze–thaw cycles.

3.2.2. Changes in Porosity and Permeability

The effective porosity of sandstone can be determined by gas porosity testing and nuclear magnetic resonance (NMR) measurements. After freeze–thaw cycling, the internal pore structure of the sandstone specimens further developed, expanded, and became interconnected under the action of frost-heaving pressure, indicating changes in the pore structure. The variations in porosity and permeability with the number of freeze–thaw cycles are shown in Figure 7. Porosity and permeability were measured after 0, 5, 10, and 15 freeze–thaw cycles. The measured apparent volume of the sandstone specimens was

25.12 cm^3. The average pore volumes were 2.67, 2.84, 2.96, and 3.12 cm^3, respectively; the average gas-measured porosities were 10.63%, 11.34%, 11.93%, and 12.45%, respectively; the average NMR-derived porosities were 9.91%, 11.14%, 11.73%, and 12.29%, respectively; and the average permeabilities were 0.28, 0.42, 0.73, and 0.96 mD, respectively. These variations are consistent with the findings of Jia et al. (2020), who observed the evolution of sandstone pore structure and an overall increase in permeability under freeze–thaw cycling using nuclear magnetic resonance (NMR) techniques [11]. These findings suggest that freeze–thaw cycling promotes the transition of the sandstone pore structure from small pores toward medium and large pores, accompanied by the progressive expansion of pore throats, thereby enhancing pore connectivity and permeability. With increasing numbers of freeze–thaw cycles, both the porosity and permeability of the sandstone specimens exhibited a gradual increasing trend.

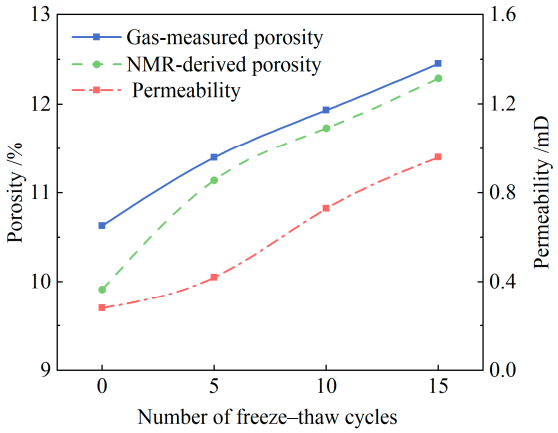


Figure 7. Variations in porosity and permeability of sandstone with the number of freeze–thaw cycles.

3.2.3. Changes in Mass and P-Wave Velocity

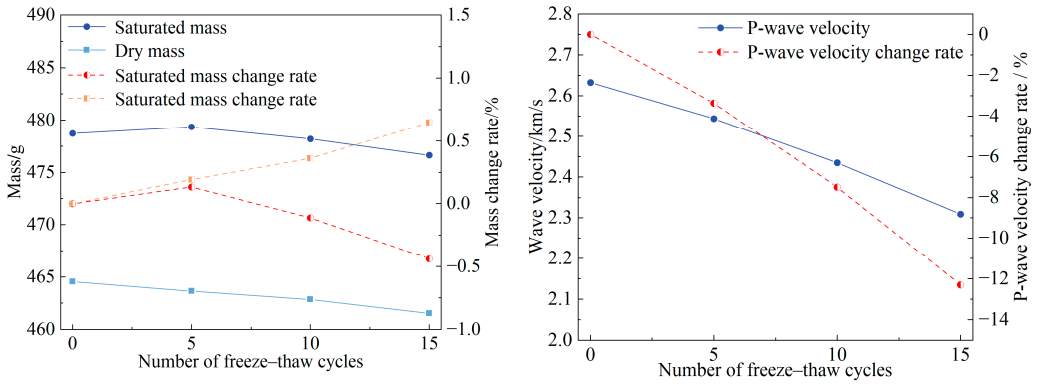
Standard sandstone specimen S7 was subjected to freeze–thaw cycling. After the specified number of cycles, the specimen was oven-dried at 105 °C for 48 h. The dry mass, saturated mass, and P-wave velocity were measured after different numbers of freeze–thaw cycles. The results are presented in Table 3, and the corresponding rates of change are shown in Figure 8. As shown in the figure, the dry mass of specimen S7 gradually decreased from an initial value of 464.53 g to 463.64, 462.85, and 461.52 g after 5, 10, and 15 freeze–thaw cycles, respectively. In contrast, the saturated mass initially increased from 478.71 g to 479.34 g after 5 cycles, and subsequently decreased to 478.18 and 476.61 g after 10 and 15 cycles, respectively. With increasing numbers of freeze–thaw cycles, the dry mass of the sandstone continuously decreased, whereas the saturated mass initially increased and then decreased. During the early stage of freeze–thaw cycling, frost-heaving effects caused by the phase transition of pore water promoted the expansion of pre-existing pores and microcracks. This increased the water-storage capacity of the specimen, resulting in a slight increase in saturated mass after 5 cycles. As freeze–thaw cycling continued, pores and cracks further expanded and gradually became interconnected, accompanied by grain detachment. These changes resulted in a gradual decrease in specimen mass. After 15 freeze–thaw cycles, the dry mass and saturated mass of specimen S7 decreased by 0.65% and 0.44%, respectively. Meanwhile, the P-wave velocity of the sandstone continuously decreased with increasing numbers of freeze–thaw cycles. The average P-wave velocity of specimen S7 gradually decreased from an initial value of 2.632 km/s to 2.544, 2.435, and 2.309 km/s after 5, 10, and 15 cycles, respectively, corresponding to a reduction

of 12.30% after 15 cycles. This decrease can be attributed to the continuous expansion, development, and interconnection of internal pores and microcracks under repeated freeze–thaw action. These structural changes weakened the integrity of the rock and increased the scattering and attenuation of elastic waves during propagation.

Therefore, both the mass loss and the decrease in P-wave velocity of the sandstone specimen reflect the pronounced cumulative damage induced by freeze–thaw cycling, with P-wave velocity exhibiting a relatively sensitive response to internal structural deterioration.

Table 3. Statistical results of mass and p-wave velocity of sandstone specimens under freeze–thaw cycling.

Specimen No.	Number of Freeze–Thaw Cycles	Mass (g)		P-Wave Velocity (km/s)				
		Dry/Saturated	Rate of Change (%)	Test 1	Test 2	Test 3	Average	Rate of Change (%)
S7	0	464.53/478.71	–	2.632	2.577	2.688	2.632	–
	5	463.64/479.34	−0.19/0.13	2.577	2.551	2.504	2.544	−3.36
	10	462.85/478.18	−0.36/−0.11	2.451	2.427	2.427	2.435	−7.50
	15	461.52/476.61	−0.65/−0.44	2.358	2.232	2.336	2.309	−12.30



(**a**) Variation in mass (**b**) Variation in p-wave velocity

Figure 8. Variations in mass and p-wave velocity of sandstone specimens under freeze–thaw cycling.

3.3. Pore Structure Evolution Characteristics of Sandstone Based on NMR

3.3.1. T_2 Spectrum Distribution and Pore Proportion Characteristics

Nuclear magnetic resonance (NMR) scanning was performed on sandstone specimens subjected to different numbers of freeze–thaw cycles, and their pore distributions were calculated. According to the pore-size distribution characteristics, the pores in the specimens were classified into three categories: micropores ($r < 0.1$ μm), mesopores (0.1 μm $\leq r < 10$ μm), and macropores ($r \geq 10$ μm). The variations in the proportions of pores with different pore sizes and the fractal dimension with the number of freeze–thaw cycles were further analyzed, as shown in Figure 9.

As shown in Figure 9a, the T_2 spectrum of the sandstone before freeze–thaw cycling is mainly characterized by a distinct single dominant peak, with peak P_1 being predominant. After freeze–thaw cycling, a secondary peak P_2 gradually appears in the region of shorter relaxation times, and the T_2 spectrum evolves from a single dominant peak to a bimodal distribution. Meanwhile, the positions, amplitudes, and spectral areas of both the main peak and secondary peak change to varying degrees. The cumulative porosity

continuously increases with increasing numbers of freeze–thaw cycles, indicating that freeze–thaw action promotes pore development and pore-size structure adjustment within the sandstone.

As shown in Figure 9b, freeze–thaw cycles significantly altered the proportions of pores at different scales. Compared with the specimen before freeze–thaw cycling, after 5, 10, and 15 freeze–thaw cycles, the proportion of micropores increased by 26.7% and 6.7% and decreased by 6.7%, respectively; the proportion of mesopores decreased by 6.3%, 5.1%, and 5.1%, respectively; and the proportion of macropores increased by 16.7%, 50.0%, and 83.3%, respectively. During the initial stage of freeze–thaw cycling, pre-existing microdefects expanded and new micropores formed, resulting in a marked increase in the proportion of micropores. As freeze–thaw cycling continued, some micropores and mesopores further expanded and became interconnected, gradually transforming into larger pores. Consequently, the proportion of micropores decreased, whereas the proportion of macropores continued to increase. These results indicate that freeze–thaw action not only increases the pore space within the sandstone but also promotes the transition of the pore structure from smaller to larger scales.

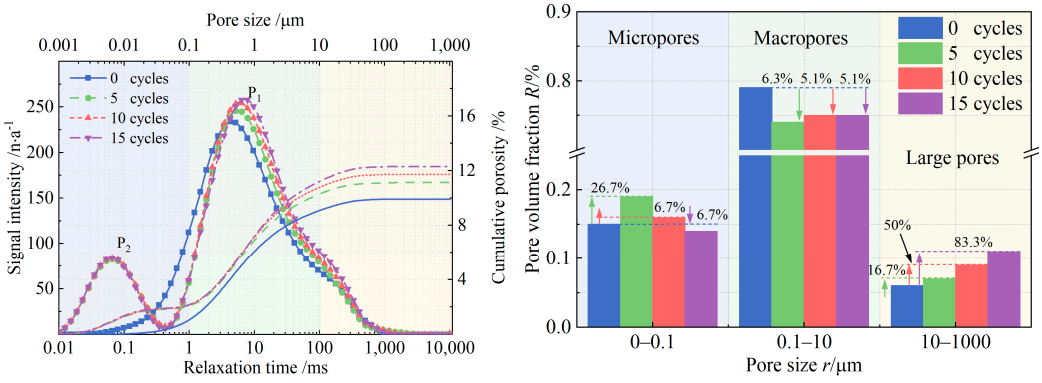
To further characterize the changes in pore structures at different scales, fractal theory was adopted based on the Brooks–Corey model [23,24]. The cumulative volume fraction, *S*v, of pores with radii smaller than *R* can be calculated using Equation (1), and an expression for the fractal dimension characterizing the pore structure can be derived from the nuclear magnetic resonance transverse relaxation time (T_2), as given in Equation (2).

$$S_v = \left(R/R_{\max}\right)^{3-D_a} \tag{1}$$

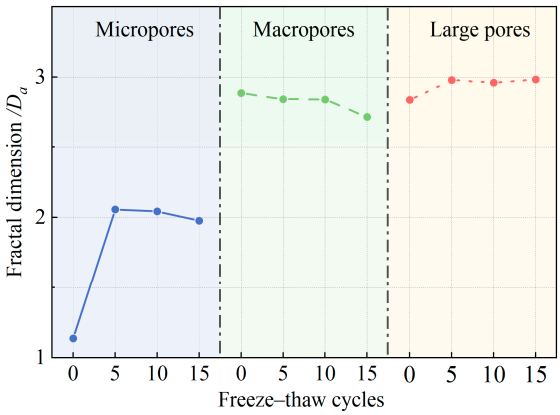
$$\lg S_v = \left(3-D_a\right)\lg\left\{T_2\right\}_s + \left(D_a-3\right)\lg\left\{T_{2,\max}\right\}_s \tag{2}$$

where R_{max} is the maximum pore radius and $T_{2,\,max}$ is the maximum transverse relaxation time.

According to Equation (2), the pore-structure fractal dimension, *D*a, was calculated. As shown in Figure 9c, the fractal dimension of micropores initially increased and then gradually decreased with increasing numbers of freeze–thaw cycles, whereas those of mesopores and macropores gradually increased. These results further demonstrate that freeze–thaw cycling promotes pore development in the sandstone, resulting in a more complex microstructure.



(**a**) T_2 spectrum curves and porosity evolution (**b**) Evolution of pore proportions



(**c**) Evolution of pore fractal dimensions

Figure 9. Pore structure evolution of sandstone after different numbers of freeze–thaw cycles.

3.3.2. NMR Imaging Characteristics

To further reveal the spatial evolution characteristics of the internal pore structure of sandstone under freeze–thaw cycling, layered NMR imaging tests were conducted by selecting three regions along the axial direction of the specimens, namely the upper, middle, and lower regions. The results are shown in Figure 10. In the NMR images, color variations reflect differences in the signal intensity of pore fluids. The colors ranging from blue to red represent the intensity of pore fluid signals, where blue corresponds to low-signal regions, indicating a relatively low local pore fluid content, while red corresponds to high-signal regions, indicating stronger local pore fluid signals. The numerical values on the color scale represent the relative NMR signal intensity acquired by the measurement system. These digitally quantified signal intensities are dimensionless and are therefore expressed in arbitrary units (a.u.).

As shown in Figure 10, the cross-sections of sandstone without freeze–thaw cycling were mainly characterized by low-signal regions. Only a small number of localized high-signal regions existed inside the specimens, and their distributions were relatively uniform among the upper, middle, and lower sections. This indicates that the internal pore space of the sandstone was relatively limited in the initial state and that the overall structure was relatively dense, although a certain degree of initial heterogeneity still existed. After 5 freeze–thaw cycles, scattered green and yellow spots appeared in the cross-sectional images, mainly in the central regions or edge transition zones, and the boundary contours of the sandstone specimens became increasingly distinct. In particular, the density of bright spots in the middle cross-section increased significantly and exhibited an uneven distribution, indicating that pre-existing weak damage zones were preferentially activated. This indicates that the pore water signal intensity increased and became unevenly distributed at this stage. Freeze–thaw action induced crack propagation and pore enlargement, causing the pore structure to evolve from a relatively homogeneous state toward a heterogeneous state. Microcracks began to initiate within the sandstone, marking the onset of the early expansion stage. After 10 freeze–thaw cycles, the area of high-density bright regions in the cross-sectional images further expanded, and the bright regions in the central and outer areas gradually became connected. Locally, yellow clusters merged into continuous regions, indicating increased pore interconnection and connectivity within the sandstone, the formation of a fracture network, and further development of the expansion process. After 15 freeze–thaw cycles, the cross-sectional images exhibited densely distributed high-intensity bright spots, indicating a significant increase in the internal porosity of the sandstone. A large number of microcracks initiated and gradually

became interconnected, resulting in increased complexity of the pore structure and the development of a planar expansion stage.

In summary, the layered NMR imaging results indicate that, with increasing numbers of freeze–thaw cycles, the overall intensity of pore-fluid signals within the sandstone increased. The high-signal regions gradually evolved from locally discrete distributions toward broader and more concentrated distributions, indicating that freeze–thaw action promoted the expansion of internal pore spaces and enhanced pore connectivity. These results are consistent with and corroborate the aforementioned T_2 spectrum analysis, porosity measurements, and pore-size distribution evolution, further demonstrating that freeze–thaw cycling accelerates the accumulation of internal damage in sandstone through continuous changes in pore-structure characteristics.

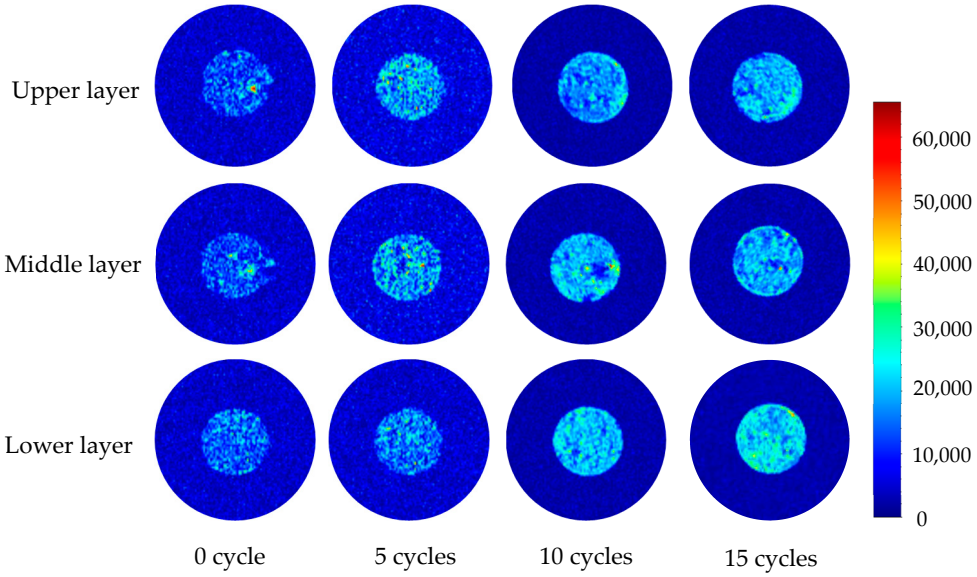


Figure 10. Layered NMR images of sandstone after different numbers of freeze–thaw cycles.

3.4. Evolution of the Three-Dimensional Pore Structure of Sandstone Based on CT Scanning

Each intact sandstone specimen was scanned four times after being subjected to different numbers of freeze–thaw cycles. Each scan produced 16-bit grayscale images with a resolution of 1000 × 1000 pixels for subsequent analysis. The CT scanning acquisition parameters are presented in Table 4.

Table 4. CT scanning acquisition parameters.

SOD (mm)	SDD (mm)	Voltage (kV)	Current (mA)	Exposure Time (s)	Spatial Resolution (μm)
535	903	115	0.28	0.85	35

Porosity and permeability are important parameters for characterizing the connectivity of the internal pore structure of sandstone and are closely related to its intrinsic structural characteristics. Because freeze–thaw cycling has a pronounced influence on the pore structure of the sandstone investigated in this study, this section quantitatively describes and evaluates the changes in the internal mesostructure of sandstone specimens after different numbers of freeze–thaw cycles based on variations in porosity, pore number, interconnected porosity, throat length, permeability, and fractal dimension. During freeze–thaw cycling, the pre-existing pore structure within the rock undergoes continuous development, propagation, and further interconnection, while new pores are also gradually initiated. These changes can generally be characterized by the interconnected porosity, P_0, and the effective pore diameter, d. Therefore, interconnected porosity can be used

to characterize the development of freeze–thaw-induced damage in the tested rock specimens. In addition, using the pore-network-modeling (PNM) module, the three-dimensional pore structures of sandstone after different numbers of freeze–thaw cycles can be visualized using a sphere-and-stick model. A schematic representation of the model is shown in Figure 11, in which the spheres represent pores and the sticks connecting the spheres represent throats. Throat length describes the length of the channels connecting adjacent pores in the pore network. Together with throat radius and pore connectivity, it can be used to characterize the spatial connections within the pore network and changes in fluid transport pathways. Fractal dimension characterizes the geometric complexity of the pore structure. Its variation reflects changes in pore morphology associated with pore expansion, coalescence, and interconnection during freeze–thaw cycling.

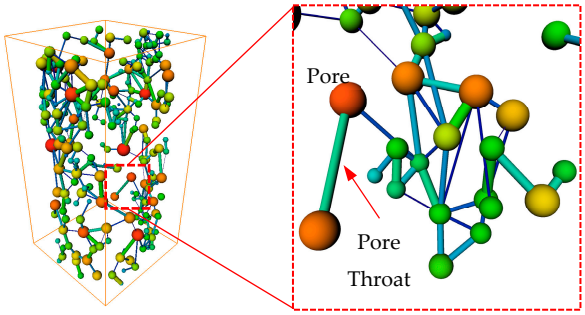


Figure 11. Schematic diagram of the sphere–stick model.

Figure 12 shows the pore segmentation results obtained from CT scans of sandstone after different numbers of freeze–thaw cycles. With increasing numbers of freeze–thaw cycles, the pore structures observed in the CT slice images changed markedly, accompanied by a pronounced increase in porosity. The total areal porosity, connected areal porosity, and connected pore volume fraction of the sandstone slices after different numbers of freeze–thaw cycles were calculated, and the results are shown in Figure 13. With increasing numbers of freeze–thaw cycles, the total areal porosity (S_{Tot}), connected areal porosity (S_{Con}), and connected pore volume fraction ($S_{C\text{-}T}$) at different slice positions all exhibited gradually increasing trends. These results indicate that freeze–thaw action not only increased the pore content but also promoted the transformation of isolated pores into connected pores. Meanwhile, the fluctuations in the *S*C-T curves gradually became less pronounced with increasing numbers of freeze–thaw cycles, suggesting that the pore structure tended toward a relatively stable expansion state during the later stage of freeze–thaw damage development. As shown in Figure 14, with increasing numbers of freeze–thaw cycles, the volumetric porosity of the intact sandstone gradually increased from 9.70% to 13.33%, with corresponding growth rates of 15.15%, 8.97%, and 13.30%, respectively. The connected porosity increased from 2.25% to 10.40%, with corresponding growth rates of 110.22%, 111.56%, and 140.44%, respectively. These results demonstrate that freeze–thaw cycling promoted the development of pores within the sandstone.

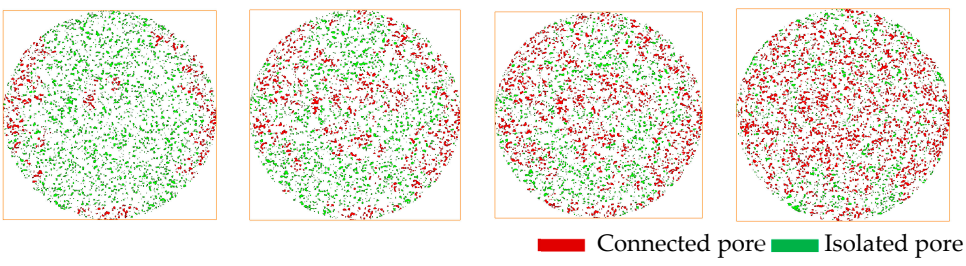
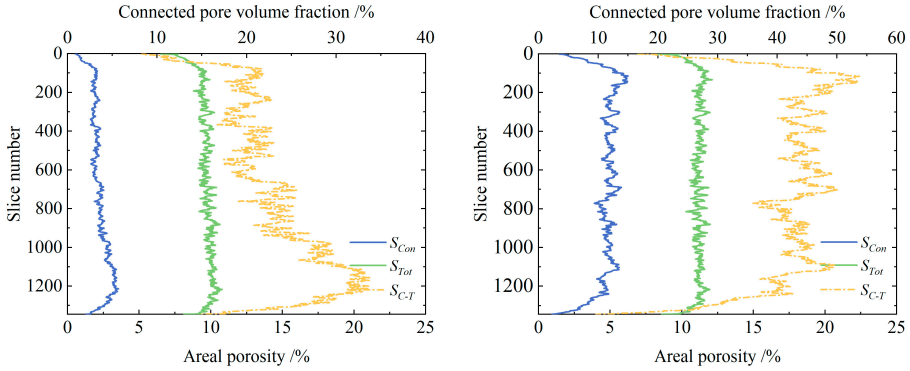


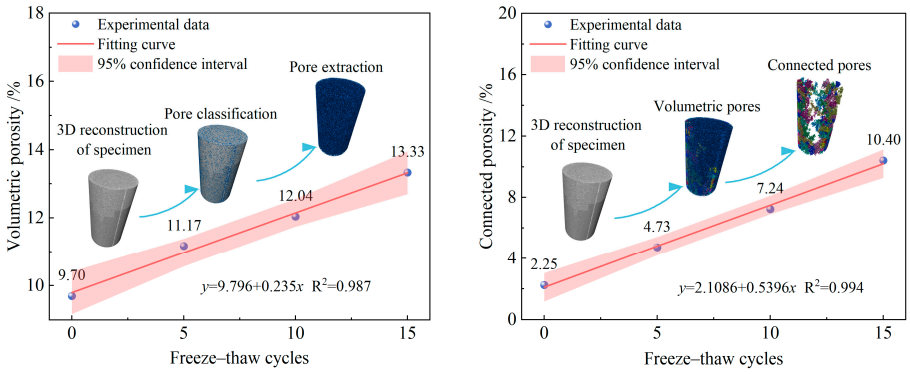
Figure 12. Pore extraction from two-dimensional CT slices of sandstone after different numbers of freeze–thaw cycles.



(**a**) 0 freeze–thaw cycles (**b**) 5 freeze–thaw cycles

(**c**) 10 freeze–thaw cycles (**d**) 15 freeze–thaw cycles

Figure 13. Variation in the areal porosity of sandstone with slice number after different numbers of freeze–thaw cycles.



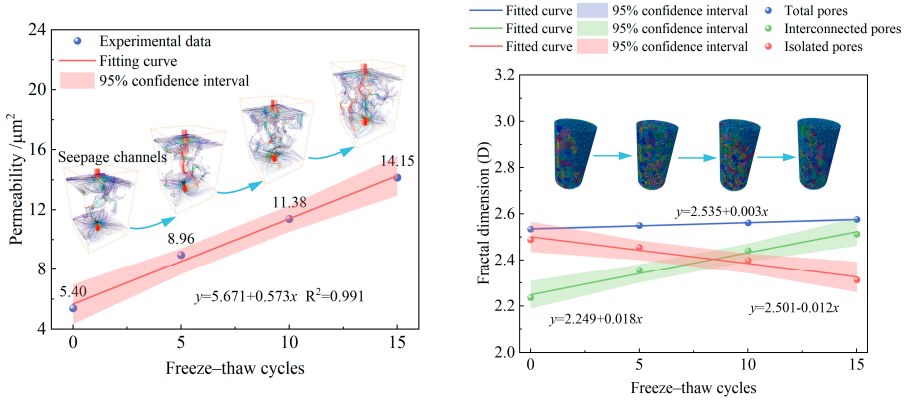
(**a**) Variation in volumetric porosity (**b**) Variation in connected porosity

Figure 14. Variation in the volumetric porosity of sandstone with the number of freeze–thaw cycles.

Figure 15 shows the variations in sandstone permeability and fractal dimension with the number of freeze–thaw cycles. After freeze–thaw cycling, the permeability of the sandstone continuously increased from 5.40 μm² before freeze–thaw cycling to 14.15 μm² after 15 freeze–thaw cycles. After different numbers of freeze–thaw cycles, the permeability values were 1.66, 2.11, and 2.62 times that of the sandstone before freeze–thaw cycling, respectively (Figure 15a). Fitting of the permeability data showed that sandstone permeability exhibited a positive linear correlation with the number of freeze–thaw cycles. The increase in permeability further indicates that, when saturated sandstone freezes, the

volumetric expansion of pore and fracture water during the water–ice phase transition induces stress concentration, thereby promoting the expansion, propagation, and interconnection of the internal pore structure. Macroscopically, these changes are manifested as an increase in sandstone permeability.

Figure 15b presents the calculated fractal dimensions of the total pores, connected pores, and isolated pores in the sandstone. As the number of freeze–thaw cycles increased, the fractal dimensions of the sandstone generally ranged from 2.24 to 2.58. The fractal dimensions of the total pores and connected pores exhibited gradual increasing trends, indicating that their morphological characteristics became increasingly complex. This trend can be explained by the evolution of the pore structure under freeze–thaw action. With repeated freeze–thaw cycling, the pre-existing pores within the sandstone continuously developed and became interconnected. The interconnection of pre-existing pores played a dominant role in pore evolution, whereas the initiation of new pores played a secondary role. Consequently, the fractal dimensions of the total pores and connected pores increased progressively, with the increase in the fractal dimension of connected pores being slightly greater than that of the total pores. In contrast, the fractal dimension of isolated pores exhibited a gradual decreasing trend, indicating that the morphology of isolated pores became progressively simpler. Therefore, the fractal dimension of isolated pores decreased progressively with increasing numbers of freeze–thaw cycles.



(**a**) Variation in permeability (**b**) Variation in fractal dimension

Figure 15. Variations in sandstone permeability and fractal dimension with the number of freeze–thaw cycles.

Figure 16 shows the total number of pores and the number of connected pores after different numbers of freeze–thaw cycles. With increasing numbers of freeze–thaw cycles, the total number of pores gradually decreased from 256,237 to 194,910, whereas the number of connected pores progressively increased from 222 to 1308. Combined with the variations in volumetric porosity and connected porosity shown in Figure 14, these results indicate that the decrease in pore number during repeated freeze–thaw cycling does not imply a reduction in pore volume. Instead, freeze–thaw damage causes the pore structure to become more fragmented overall, while the pores become larger. Specifically, the number of small pores decreases, whereas the number of large pores increases, resulting in progressive coarsening of the pore structure. These results further confirm that damage to the internal pore structure of sandstone under freeze–thaw cycling develops progressively, whereby small pores gradually interconnect and coalesce into fewer but larger pores, and may eventually develop into fractures.

Figure 17 shows the variations in the equivalent diameter, area, volume, and morphological parameters of connected pores with the number of freeze–thaw cycles. With increasing numbers of freeze–thaw cycles, the number of connected pores within the

sandstone continuously increased, the pore size progressively enlarged, and the pore morphology gradually evolved from relatively regular to increasingly irregular forms. These results indicate that freeze–thaw action exerts a pronounced deterioration effect on the internal structure of the rock.

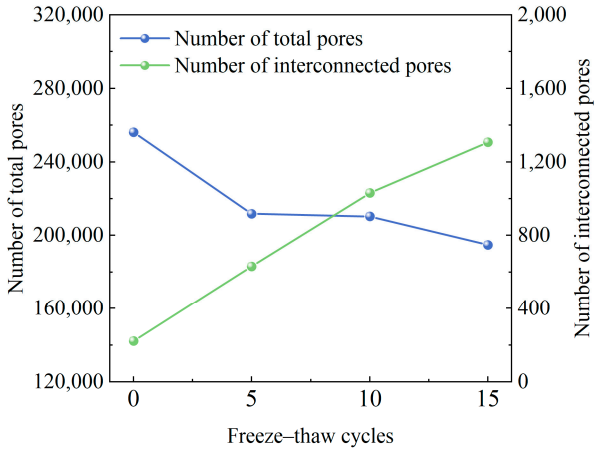
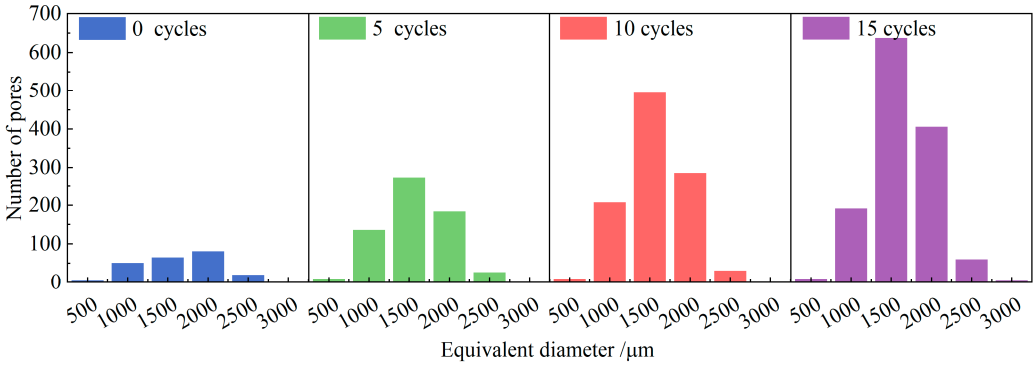


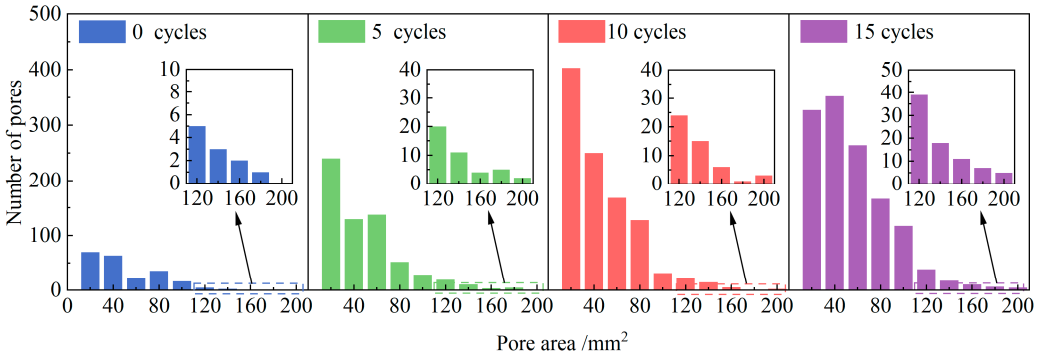
Figure 16. Variation in the number of sandstone pores with the number of freeze–thaw cycles.

As shown by the equivalent diameter distribution of connected pores (Figure 17a), the equivalent pore diameters of sandstone without freeze–thaw treatment were mainly concentrated within the smaller size range, and the number of connected pores was relatively low. After 5 or more freeze–thaw cycles, the pore-diameter distribution gradually shifted toward larger values, and the number of pores with equivalent diameters in the range of 1500–2500 μm progressively increased. After 15 freeze–thaw cycles, the pore diameters were predominantly concentrated within the larger size range, indicating that freeze–thaw cycling continuously promoted pore expansion and interconnection. The variations in pore area (Figure 17b) and pore volume (Figure 17c) were consistent with those in equivalent diameter. After 15 freeze–thaw cycles, the numbers of pores with small areas and volumes gradually decreased, whereas those of medium- and large-sized pores increased significantly, with the distributions in the bar charts clearly shifting toward larger pore areas and volumes. These results further demonstrate that freeze–thaw action promoted the expansion of pre-existing pores and induced the coalescence and interconnection of multiple pores, thereby forming larger-scale pore structures.

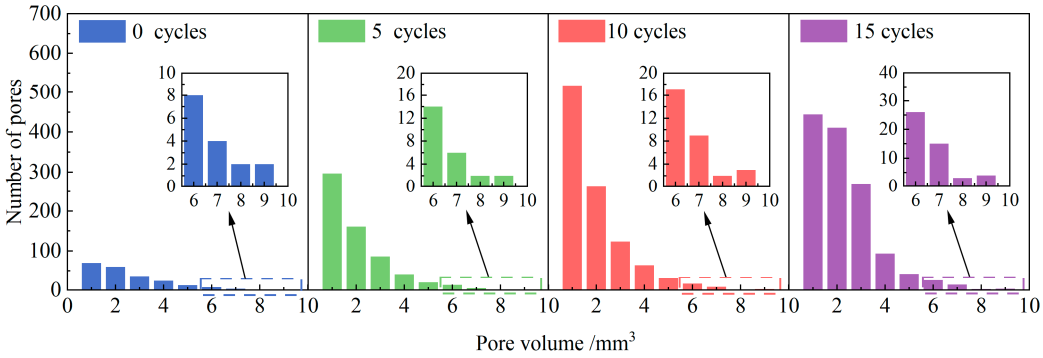
In terms of the pore shape factor (Figure 17d), its distribution also showed an overall increasing trend with increasing numbers of freeze–thaw cycles, gradually extending from the initially lower range toward higher values. This indicates that freeze–thaw action promoted the progressive development and interconnection of pores within the sandstone, while the pore morphology gradually evolved toward more irregular and angular forms. Meanwhile, the pore boundaries became increasingly fragmented, further revealing the deterioration of the internal structure of sandstone under freeze–thaw action.



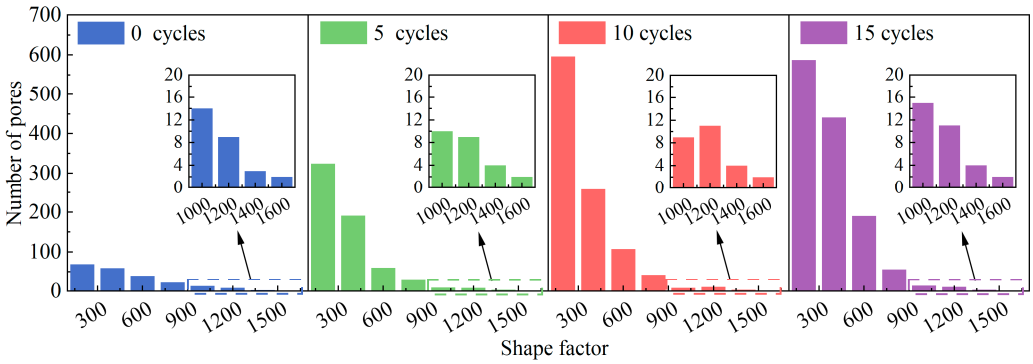
(**a**) Variation in pore equivalent diameter



(**b**) Variation in pore area



(**c**) Variation in pore volume



(**d**) Variation in pore shape factor

Figure 17. Variations in connected pore parameters of sandstone with the number of freeze–thaw cycles.

3.5. Analysis of Sandstone Failure Characteristics Under Freeze–Thaw Action

Digital image correlation (DIC) is a non-contact full-field deformation measurement technique. By tracking the displacement of speckle subsets on the specimen surface before

and after deformation, the displacement and strain fields during loading can be obtained [25,26]. Its basic principle is illustrated in Figure 18. Before testing, a uniform white base coat and a random black speckle pattern were prepared on the surface of each sandstone specimen. A high-speed camera was then used to synchronously record the entire uniaxial compression process, thereby capturing the evolution of the strain field at different loading stages (Figure 19).

In this study, a Revealer RDIC-A7A20MU201 digital image correlation (DIC) strain measurement system, manufactured by Hefei Zhongke Junda Vision Technology Co., Ltd., Hefei, China, was employed. The system was equipped with an RVM-HS-S high-speed camera for image acquisition. The camera configuration has a nominal image resolution of 1280 × 800 pixels and a maximum specified frame rate of 16,000 frames per second (fps). The nominal displacement and strain measurement accuracies of the system are ≤0.01 pixel and ≤100 με, respectively. During the experiments, the actual image acquisition frame rate was set to 10,000 fps to capture the surface deformation and crack propagation of sandstone specimens during uniaxial compression loading.

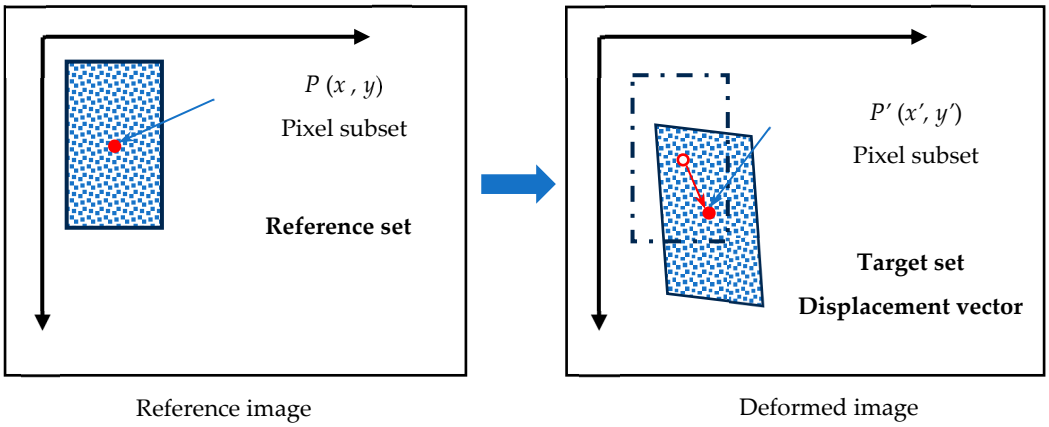


Figure 18. Principle of digital image correlation (DIC).

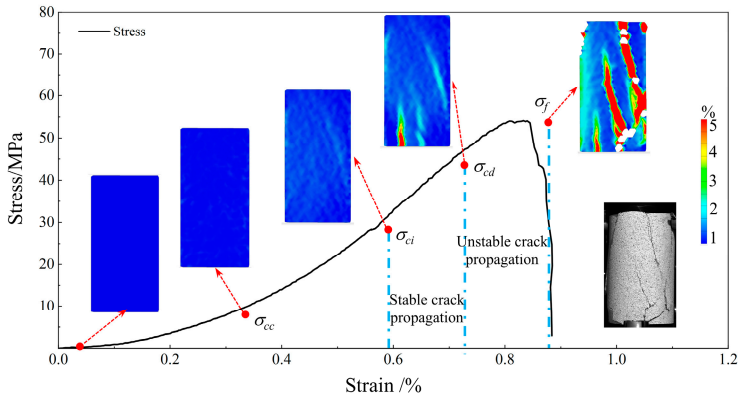
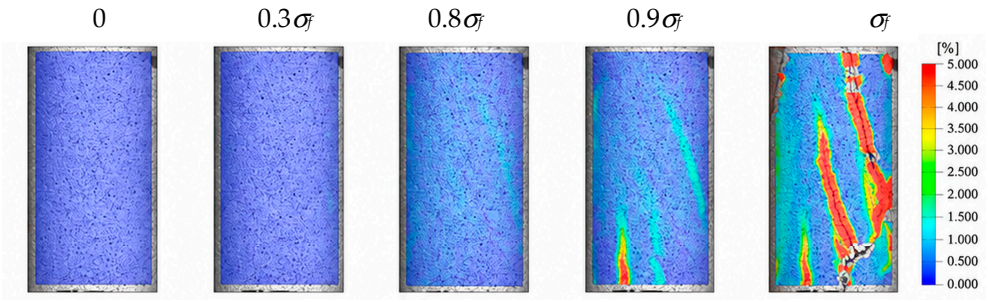


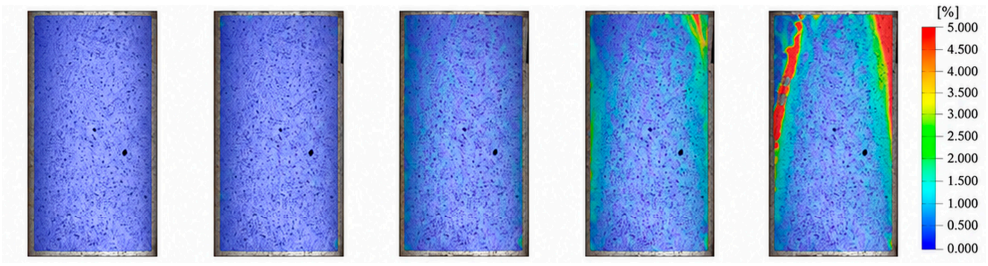
Figure 19. Stress–strain curves and DIC strain-field evolution contour maps of sandstone specimens.

Figure 20 shows the DIC strain-field evolution contour maps of intact sandstone specimens subjected to uniaxial compression after different numbers of freeze–thaw cycles. It can be observed that, at the loading stage of 0~0.3σ_f, the strain fields of all specimen groups were generally uniform, with only weak localized strain concentrations. As the number of freeze–thaw cycles increased, the number of discrete anomalous strain regions on the specimen surfaces increased, indicating that freeze–thaw action promoted the development of pre-existing pores and microcracks within the sandstone and thereby

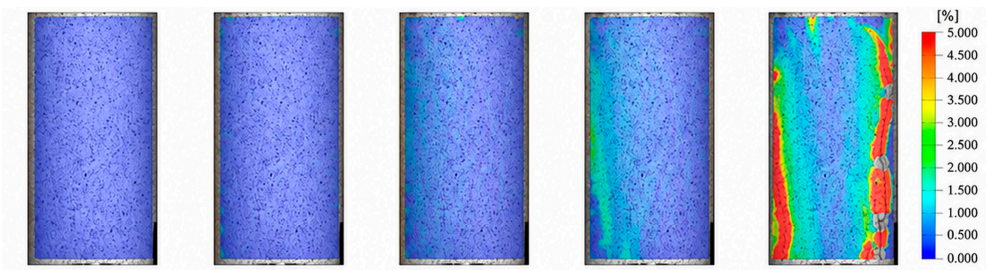
intensified the non-uniform deformation during the compaction stage. When loading continued to $0.8\sigma_f$, strain localization gradually became evident. The specimen without freeze–thaw treatment was mainly characterized by localized and discrete strain concentrations, whereas the freeze–thaw-treated specimens gradually developed distinct band-shaped high-strain regions. With increasing numbers of freeze–thaw cycles, both the length and extent of the strain concentration regions increased, with the specimen subjected to 15 freeze–thaw cycles exhibiting the most pronounced strain localization. After loading to $0.9\sigma_f$, the high-strain bands rapidly expanded and tended to become interconnected. Specimens subjected to more freeze–thaw cycles simultaneously exhibited multiple localized strain concentration regions, indicating that internal damage developed in a more dispersed and complex manner. When the load reached the peak stress σ_f, the high-strain region in the specimen without freeze–thaw treatment was relatively concentrated, forming a distinct main failure band. After 5 and 10 freeze–thaw cycles, the high-strain bands expanded in extent and exhibited a certain degree of branching. In contrast, the specimen subjected to 15 freeze–thaw cycles developed multiple intersecting high-strain bands, accompanied by localized fragmentation and spalling near the specimen ends, indicating a marked increase in the degree of failure. These results indicate that, with increasing numbers of freeze–thaw cycles, damage associated with internal pores in the sandstone continuously accumulated, causing strain localization to evolve from a relatively concentrated pattern toward coordinated development across multiple regions and ultimately resulting in increasingly complex failure modes.



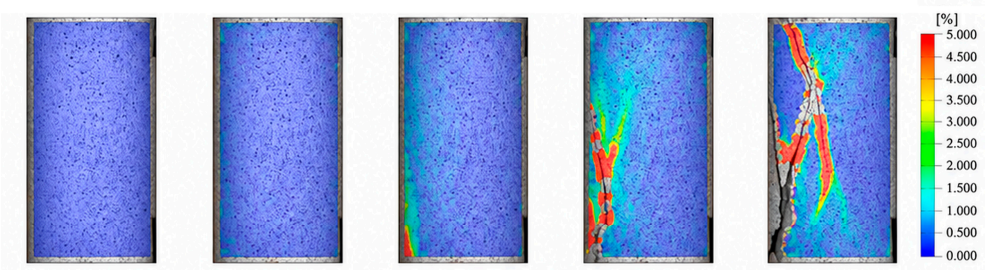
(**a**) 0 freeze–thaw cycles



(**b**) 5 freeze–thaw cycles



(**c**) 10 freeze–thaw cycles



(**d**) 15 freeze–thaw cycles

Figure 20. Failure evolution characteristics of intact sandstone specimens under uniaxial compression after different numbers of freeze–thaw cycles.

4. Conclusions

This study employed physical parameter measurements, scanning electron microscopy (SEM), nuclear magnetic resonance (NMR), computed tomography (CT), and digital image correlation (DIC) to investigate the evolution of the pore structure and multiscale damage mechanisms of sandstone under freeze–thaw cycling. The main conclusions are as follows:

(1) Freeze–thaw cycling significantly altered the macroscopic physical properties of sandstone and exhibited a pronounced cumulative damage effect. With increasing numbers of freeze–thaw cycles, the dry mass and P-wave velocity of the sandstone continuously decreased, whereas its porosity and permeability gradually increased. After 15 freeze–thaw cycles, the dry mass decreased by 0.65%, the P-wave velocity decreased by 12.30%, the gas-measured porosity increased from 10.63% to 12.45%, and the permeability increased from 0.28 mD to 0.96 mD.

(2) Freeze–thaw cycling weakened intergranular cementation, promoted microcrack propagation, and induced pore-size structure adjustment, resulting in pronounced pore coarsening. The pore structure gradually shifted from smaller pores toward medium- and large-sized pores. After 15 freeze–thaw cycles, the proportion of macropores increased by 83.3% compared with the initial state.

(3) Freeze–thaw cycling significantly enhanced pore connectivity in the sandstone, as evidenced by a decrease in the total number of pores and an increase in the number of connected pores. The volumetric porosity increased from 9.70% to 13.33%, while the connected porosity increased from 2.25% to 10.40%, indicating that isolated pores continuously expanded, coalesced, and gradually developed into an interconnected pore network.

(4) The evolution of freeze–thaw damage followed a progressive process of microdefect activation–pore expansion–crack interconnection–interconnected network reconstruction–macroscopic property deterioration. During uniaxial compression, distinct band-shaped high-strain zones gradually developed in the freeze–thaw-treated sandstone specimens when the applied stress reached 0.8 times the peak stress. At 0.9 times the peak stress, these high-strain bands further expanded and tended to interconnect. At the peak stress, the specimen without freeze–thaw treatment mainly exhibited a relatively concentrated main failure band. In contrast, the specimen subjected to 15 freeze–thaw cycles developed multiple intersecting high-strain bands. These results indicate that freeze–thaw cycling promoted the earlier onset of strain localization in sandstone and caused high-strain zones to evolve from localized concentrations toward a more distributed pattern across multiple regions.

Author Contributions: J.R.: Writing—review and editing, Funding acquisition, Conceptualization. K.Z.: Writing—original draft, Methodology, Investigation, Data curation. M.Y.: Writing—original

draft, Methodology, Investigation, Data curation. Z.J.: Writing—original draft, Data curation. H.W.: Formal analysis, Data curation. All authors have read and agreed to the published version of the manuscript.

Funding: This research was funded by the College of Architecture and Civil Engineering, Xi'an University of Science and Technology. This study was supported by the National Natural Science Foundation of China (No. 42377187 and No. 12072259) and the National Science Foundation for Young Scientists of China (No. 42507282).

Data Availability Statement: The data that support the findings of this study are available from the corresponding author upon reasonable request.

Conflicts of Interest: The authors declare no conflict of interest.

References

1. Matsuoka, N. Mechanisms of rock breakdown by frost action: An experimental approach. *Cold Reg. Sci. Technol.* **1990**, *17*, 253–270. https://doi.org/10.1016/S0165-232X(05)80005-9.
2. Matsuoka, N.; Murton, J. Frost weathering: Recent advances and future directions. *Permafr. Periglac. Process.* **2008**, *19*, 195–210. https://doi.org/10.1002/ppp.620.
3. Murton, J.B.; Peterson, R.; Ozouf, J.C. Bedrock fracture by ice segregation in cold regions. *Science* **2006**, *314*, 1127–1129. https://doi.org/10.1126/science.1132127.
4. Deprez, M.; De Kock, T.; De Schutter, G.; Cnudde, V. A review on freeze-thaw action and weathering of rocks. *Earth-Sci. Rev.* **2020**, *203*, 103143. https://doi.org/10.1016/j.earscirev.2020.103143.
5. Huang, S.B.; Ye, Y.H.; Cui, X.Z.; Cheng, A.P.; Liu, G.F. Theoretical and experimental study of the frost heaving characteristics of the saturated sandstone under low temperature. *Cold Reg. Sci. Technol.* **2020**, *174*, 103036. https://doi.org/10.1016/j.coldregions.2020.103036.
6. Zucca, M.; Landi, F.; Puppio, M.L.; Mistretta, F.; Formichi, P.; Croce, P. Climate change impact on corrosion of reinforced concrete bridges and their seismic performance. *Appl. Sci.* **2024**, *14*, 60. https://doi.org/10.3390/app14010060.
7. Li, J.L.; Kaunda, R.B.; Zhou, K.P. Experimental investigations on the effects of ambient freeze-thaw cycling on dynamic properties and rock pore structure deterioration of sandstone. *Cold Reg. Sci. Technol.* **2018**, *154*, 133–141. https://doi.org/10.1016/j.coldregions.2018.06.015.
8. Ke, B.; Zhou, K.P.; Deng, H.W.; Bin, F. NMR pore structure and dynamic characteristics of sandstone caused by ambient freeze-thaw action. *Shock Vib.* **2017**, *2017*, 9728630. https://doi.org/10.1155/2017/9728630.
9. Zhou, X.P.; Li, C.Q.; Zhou, L.S. The effect of microstructural evolution on the permeability of sandstone under freeze-thaw cycles. *Cold Reg. Sci. Technol.* **2020**, *177*, 103119. https://doi.org/10.1016/j.coldregions.2020.103119.
10. Zhang, J.Y.; Wang, G.B.; Liu, H.D.; Yang, M.M. Study on the evolution of microscopic pore structure of sandstone under freeze-thaw cycles. *Cold Reg. Sci. Technol.* **2024**, *217*, 104018. https://doi.org/10.1016/j.coldregions.2023.104018.
11. Jia, H.L.; Ding, S.; Zi, F.; Dong, Y.H.; Shen, Y.J. Evolution in sandstone pore structures with freeze-thaw cycling and interpretation of damage mechanisms in saturated porous rocks. *Catena* **2020**, *195*, 104915. https://doi.org/10.1016/j.catena.2020.104915.
12. Pan, Z.; Zhou, K.P.; Gao, R.G.; Jiang, Z.; Yang, C.; Gao, F. Research on the pore evolution of sandstone in cold regions under freeze-thaw weathering cycles based on NMR. *Geofluids* **2020**, *2020*, 8849444. https://doi.org/10.1155/2020/8849444.
13. Liu, B.; Ma, Y.J.; Liu, N.; Han, Y.H.; Li, D.Y.; Deng, H.L. Investigation of pore structure changes in Mesozoic water-rich sandstone induced by freeze-thaw process under different confining pressures using digital rock technology. *Cold Reg. Sci. Technol.* **2019**, *161*, 137–149. https://doi.org/10.1016/j.coldregions.2019.03.006.
14. Zhang, X.T.; Luo, X.D.; He, X.; Niu, S.S. Pore structure expansion and evolution in sandstone with prefabricated crack under freeze-thaw cycles based on CT scanning. *Front. Earth Sci.* **2024**, *12*, 1394731. https://doi.org/10.3389/feart.2024.1394731.
15. Che, Y.X.; Song, Y.J.; Yang, H.M.; Tan, H.; Zhang, L.T. Freeze-thaw induced structural deterioration of fractured rock: A coupled NMR–CT study on pore network evolution. *Theor. Appl. Fract. Mech.* **2026**, *141*, 105274. https://doi.org/10.1016/j.tafmec.2025.105274.
16. Song, Y.M.; Ma, S.P.; Yang, X.B.; Wang, X. Experimental investigation on failure of rock by digital speckle correlation methods. *Chin. J. Rock Mech. Eng.* **2011**, *30*, 170–175.

17. Zhao, C.; Tian, J.S.; Matsuda, H.; Zhao, C.F.; Bao, C. Study on the crack propagation and damage evolution characteristics of rock based on the global strain field under uniaxial compression. *Chin. J. Rock Mech. Eng.* **2015**, *34*, 763–769. https://doi.org/10.13722/j.cnki.jrme.2015.04.013.
18. Fan, J.; Zhu, X.; Hu, J.W.; Tang, Y.; He, C.L. Experimental study on crack propagation and damage monitoring of sandstone using three-dimensional digital image correlation technology. *Rock Soil Mech.* **2022**, *43*, 1009–1019. https://doi.org/10.16285/j.rsm.2021.1132.
19. Zhang, H.M.; Gao, P.X.; Jia, H.L.; Wang, T.; Tang, L.Y. Study on the damage localization law in frozen sandstone during uniaxial compression. *J. Glaciol. Geocryol.* **2024**, *46*, 565–577. https://doi.org/10.7522/j.issn.1000-0240.2024.0046.
20. Yang, G.L.; Shang, Z.; Zou, Z.H.; Bi, J.J.; Dong, Z.W. Study on dynamic splitting and evolution mechanism of sandstone under freeze-thaw cycle. *J. Min. Sci. Technol.* **2024**, *9*, 199–208. https://doi.org/10.19606/j.cnki.jmst.2024.02.007.
21. Zhang, C.Y.; Hu, K.B.; Zhao, E.C.; Tan, T. Crack propagation law and damage evolution characteristics of freeze-thaw fractured sandstone based on XT-DIC. *J. Liaoning Tech. Univ. (Nat. Sci.)* **2025**, *44*, 293–302. https://doi.org/10.11956/j.issn.1008-0562.20240301.
22. Qiao, C. Study on Damage Evolution Law and Disaster-Causing Mechanism of Rock Slope with Locked Segment Subjected to Freeze-Thaw Cycles. Ph.D. Thesis, University of Science and Technology Beijing, Beijing, China, 2023.
23. Brideau, M.A.; Yan, M.; Stead, D. The role of tectonic damage and brittle rock fracture in the development of large rock slope failures. *Geomorphology* **2009**, *103*, 30–49. https://doi.org/10.1016/j.geomorph.2008.04.010.
24. Bagde, M.N.; Petroš, V. Fatigue properties of intact sandstone samples subjected to dynamic uniaxial cyclical loading. *Int. J. Rock Mech. Min. Sci.* **2005**, *42*, 237–250. https://doi.org/10.1016/j.ijrmms.2004.08.008.
25. Cui, J.Q.; Feng, G.R.; Li, Z.; Han, Y.N.; Song, C.; Niu, X.H.; Wen, X.Z. Failure analysis of sandstone with filled and unfilled cross-flaws under uniaxial compression. *Arab. J. Sci. Eng.* **2022**, *47*, 13435–13449. https://doi.org/10.1007/s13369-022-06839-w.
26. Chen, Y.F.; Tang, Y.; Cao, R.H.; Sun, S.W.; Zha, W.H.; Lin, H. Failure mode of parallel-fractured rock-like sample with different inclinations. *Theor. Appl. Fract. Mech.* **2023**, *127*, 104053. https://doi.org/10.1016/j.tafmec.2023.104053.

Disclaimer/Publisher's Note: The statements, opinions and data contained in all publications are solely those of the individual author(s) and contributor(s) and not of MDPI and/or the editor(s). MDPI and/or the editor(s) disclaim responsibility for any injury to people or property resulting from any ideas, methods, instructions or products referred to in the content.